Journal of Advanced Ceramics
先进陶瓷
ISSN 2226-4108
CN 10-1154/TQ
清华大学出版社 Tsinghua University Press
SciOpen

J Adv Ceram 2026, **15**: 9221409

https://doi.org/10.26599/JAC.2026.9221409

Research Article

K/Ce/Sm multiple-doped $CaBi_2Nb_2O_9$ aurivillius-type ceramics used for high-temperature piezoelectric ultrasonic transducer

Chengxin Xu[1,#], Junnan Wang[1,#], Huajiang Zhou[1], Jiageng Xu[1], Zhi Zhou[2], He Qi[2], Jun Chen[2], Yu Chen[3,*]

[1]*School of Mechanical Engineering, Chengdu University, Chengdu 610106, China*

[2]*School of Materials Science and Engineering, Hainan University, Haikou, China*

[3]*School of of Materials Science and Engineering, Xihua University, Chengdu 610039, China*

[#]These authors contributed equally to this work.

[*] Corresponding author.

E-mail: chenyuer20023@163.com

Received: September 29, 2026; Revised: October 29, 2026; Accepted: November 14, 2026

©The Author(s) 2026

Just Accepted

Abstract: Aurivillius-type $CaBi_2Nb_2O_9$ (CBN) is attractive for high-temperature ultrasonic sensing owing to its high Curie temperature ($T_C \approx 940$ ℃). However, its weak piezoelectric response and loss of polarization alignment during thermal exposure limit its practical performance. Herein, K/Ce/Sm co-substitution at the Ca site was employed to modify the lattice structure, electrical transport, and domain morphology of CBN ceramics. Co-substitution reduced the orthorhombic distortion while preserving the orthorhombic framework. The optimized CBN-KCS-12 ceramic exhibited a piezoelectric coefficient d_{33} of 18 pC/N, a T_C of approximately 933 ℃, and a ρ_{dc} resistivity of 2.59×10^6 Ω·cm at 650 ℃, approximately 18.5 times that of undoped CBN. The annealing temperature corresponding to 50% retention of the initial d_{33} increased from 600 to 850 ℃, and CBN-KCS-12 retained approximately 44% of its initial d_{33} after annealing at 900 ℃. Piezoresponse force microscopy revealed larger block-like regions in CBN-KCS-12 compared with the fine stripe-like patterns in undoped CBN, with block-like contrast also observed after annealing at 900 ℃. The elastic modulus also increased from 30.1 to 33.8 GPa. Finally, a single-element ultrasonic transducer fabricated from CBN-KCS-12 produced clear pulse-echo signals from room temperature to 400 ℃, achieving a signal-to-noise ratio above 36 dB and a -6 dB fractional bandwidth of approximately 42% at 400 ℃. These results demonstrate the potential of multi-element A-site co-substitution for improving CBN ceramics for high-temperature ultrasonic applications.

Keywords: $CaBi_2Nb_2O_9$; Piezoelectric ceramics; Ferroelectric domains; Thermal depolarization; High-temperature ultrasonic transducer

Just Accepted

1. Introduction

Deep-earth oil and gas exploration, advanced energy systems, and aerospace equipment demand in situ sensing and nondestructive evaluation that operates reliably under sustained high temperatures, high pressures, and intense vibration[1][5]. Ultrasonic transducers are particularly attractive in such environments because their piezoelectric active elements directly interconvert electrical and mechanical energy, enabling sensitive and rapid acoustic interrogation[6][10]. In a high-temperature transducer, the active element must maintain its polarization, suppress dielectric and conduction losses, and preserve electromechanical coupling as temperature rises[11][20].

$CaBi_2Nb_2O_9$ (CBN), a representative Aurivillius-type ferroelectric ceramic, is a promising

candidate for high-temperature piezoelectric applications because of its high Curie temperature (T_C = 940 ℃). However, a high T_C does not necessarily ensure the retention of the macroscopic piezoelectric response after thermal exposure, because the polarization alignment established during poling can deteriorate below the ferroelectric-paraelectric transition. In addition, undoped CBN exhibits a low piezoelectric coefficient (d_{33} = 5 pC/N), limiting acoustic-electrical conversion efficiency[21][24]. Its strongly anisotropic layered structure and high coercive field hinder polarization switching and effective domain alignment during poling[25][27]. These limitations motivate compositional modification to improve both the initial piezoelectric response and its retention after thermal treatment.

A-site substitution provides a route to modifying both the lattice structure and defect chemistry of bismuth layer-structured ferroelectrics. Changes in lattice distortion can affect polarization switching, while aliovalent substitution can modify charge compensation and high-temperature electrical transport[28][32]. These effects are relevant to both poling efficiency and thermal depolarization. The central scientific question is how A-site compositional modification can facilitate polarization alignment during poling while limiting the loss of piezoelectric response upon subsequent heating. Addressing this question requires examining structural evolution, electrical conduction, and domain morphology together with the measured piezoelectric retention.

In this work, a multi-element A-site co-substitution strategy was developed to address the trade-off between piezoelectric activity and thermal stability in $CaBi_2Nb_2O_9$ (CBN) ceramics. K, Ce, and Sm were introduced at the Ca site to jointly modify the lattice distortion, defect chemistry, and domain configuration. Their effects on the crystal structure, microstructure, chemical states, electrical conduction, electromechanical coupling, and thermal depolarization were systematically investigated. Co-substitution reduced the orthorhombic distortion while preserving the orthorhombic framework, accompanied by improved piezoelectric activity and high-temperature electrical insulation. PFM observations revealed a change from fine stripe-like patterns in undoped CBN to larger block-like regions in the optimized composition, providing insight into the relationship between domain morphology and piezoelectric retention after annealing. The optimized CBN-KCS-12 ceramic achieved a d_{33} of 18 pC/N and a depolarization temperature of 850 ℃ while retaining a high T_C of approximately 933 ℃. Furthermore, an ultrasonic transducer fabricated from this composition delivered clear pulse-echo signals up to 400 ℃. These findings connect

Just Accepted

compositional modification, domain evolution, and functional performance, demonstrating the potential of K/Ce/Sm co-substituted CBN ceramics for high-temperature ultrasonic sensing.

2. Experimental details

2.1 Sample preparation

$Ca_{1-x}(K_{0.5}Ce_{0.25}Sm_{0.25})_xBi_2Nb_2O_9$ (abbreviated as CBN-KCS-100x, x = 0-0.14) ceramics were prepared by a two-step conventional solid-state reaction. Stoichiometric amounts of Bi_2O_3 (99%), CeO_2 (99.99%), Sm_2O_3 (99%), Nb_2O_5 (99.99%), $CaCO_3$ (99%), and K_2CO_3 (99%) were ball-milled for 6 h in alcohol with zirconia balls, dried, and calcined at 850 ℃ for 4 h. The calcined powders were ground for 12 h, granulated with polyvinyl alcohol (PVA), and pressed into 10-mm-diameter, 0.8-mm-thick discs under an isostatic pressure of 13 MPa. After PVA burnout at 650 ℃ for 2 h, the discs were sintered in sealed alumina crucibles at 1120 ℃ for 2 h in air. The sintered ceramics were polished, coated with silver paste on both sides, fired at 700 ℃ for 10 min, and poled in a silicone-oil bath at 150 ℃ under 10 kV/mm for 30 min. All compositions were prepared and poled under the same conditions to facilitate comparison of their composition-dependent properties.

2.2 Sample characterization

The phase structure was characterized by X-ray diffraction (XRD, D8 Focus, Bruker, Germany) with Cu Kα radiation. The microstructure and elemental distribution were examined by scanning electron microscopy (SEM, JIB-4700F, JEOL, Japan) and energy-dispersive X-ray spectroscopy (EDS). X-ray photoelectron spectroscopy (XPS) was used to characterize the surface chemical states of the constituent elements. The O1s and Ce3d spectra were analyzed to examine the surface oxygen environments and Ce oxidation states, respectively. The average grain size was obtained from the linear fitting of probability plots. The local ferroelectric domain structures were characterized by piezoresponse force microscopy (PFM, Cypher ES, Asylum Research, Oxford Instruments) in contact mode using a Ti/Ir-coated conductive silicon probe (ASYELEC-01-R2) with a nominal spring constant of 2.8 N/m and a nominal tip radius of 25 nm. PFM imaging was performed at an excitation voltage of 5 V and an excitation frequency of 10 kHz, with a scan rate of 2 Hz. Both out-of-plane and in-plane PFM amplitude and phase images were simultaneously acquired together with AFM topography to correlate domain morphology with surface microstructure. For PFM measurements, polished samples were examined at room temperature before and after annealing.

Just Accepted

For the post-annealing measurements, the samples were annealed at 900 ℃ for 2 h in air, naturally cooled to room temperature, and measured without repoling. For the depolarization measurements, poled samples were annealed at different temperatures for 2 h in air, cooled naturally, and their d_{33} was remeasured at room temperature; each point is the average of three samples. The piezoelectric coefficient d_{33} was measured with a quasi-static d_{33} meter (ZJ-6AN, IACAS, China). The temperature-dependent dielectric permittivity ε_r and loss tangent tanδ were measured with a broadband LCR meter (TH2829A, Tonghui Electronics, China) attached to a programmable furnace; the electromechanical resonance characteristics were recorded from 20 Hz to 2 MHz, and the planar electromechanical coupling factor k_p, mechanical quality factor Q_m, and planar frequency constant Np were determined according to Onoe's equations[33]. The temperature-dependent DC resistivity ρ_{dc} was measured by applying 100 V across the samples using an electrometer (Keithley 6517B, Tektronix, USA) attached to a programmable furnace.

Mechanical properties were evaluated by nanoindentation and uniaxial compression. Before nanoindentation, the sintered discs were mirror-polished. Nanoindentation was performed on a KLA iNano nanoindenter (KLA Instruments, USA) with a three-sided pyramidal Berkovich diamond indenter. The tests were run in load-controlled mode at peak loads of 10, 20, 30, 40, and 50 mN, with an indentation strain rate of 0.2 s^{-1} and a drift rate of 0.1 N s^{-1}. At each peak load, a 5 × 5 array with a 50-μm spacing was used; this spacing is about an order of magnitude larger than the maximum indentation depth and prevents overlap of the deformation fields. The maximum depth h_m and residual depth h_p were extracted from the load-displacement curves. Uniaxial compression tests were performed on rectangular specimens (15 × 2 × 2 mm^3) with a Shimadzu AGS-X 10 kN universal testing machine (Shimadzu, Japan). A 1 MPa preload was applied, and the specimens were loaded under displacement control at 1 mm min^{-1} to a maximum stress of 100 MPa. The elastic modulus was determined from the slope of the linear elastic segment of the stress-strain curve.

2.3 Transducer fabrication and pulse-echo measurements

An ultrasonic transducer was fabricated using the optimized CBN-KCS-12 ceramic as the active transmitting and receiving element with fired-on silver electrodes. The transducer had a three-layer configuration consisting of a matching layer, a piezoelectric layer, and a backing layer. Specifically, the matching layer was composed of an epoxy-alumina composite designed for quarter-

Just Accepted

wave acoustic impedance matching, the piezoelectric layer employed the CBN-KCS-12 ceramic disc, and the backing layer was prepared from an epoxy-tungsten composite for acoustic attenuation. The CBN-KCS-12 ceramic element was lapped to a thickness of approximately 0.1 mm and a diameter of 9 mm, corresponding to a fundamental thickness-mode resonance frequency of ~13 MHz. The transducer housing was made of a cylindrical brass shell, and all internal components were assembled with high-temperature-resistant epoxy adhesive.

Ultrasonic pulse-echo measurements were conducted using a pulser/receiver system (DPR 300, JSR Ultrasonics, Imaginant, USA). An alumina ceramic plate approximately 10 mm thick served as the acoustic reflector. The transducer was mechanically clamped against the reflector to establish direct dry-contact acoustic coupling, without an additional coupling medium. Both the transducer and the reflector were placed inside a box-type muffle furnace and heated simultaneously by radiation from the furnace heating elements. The furnace temperature was regulated by a built-in PID controller. Measurements were performed from room temperature to 400 ℃, with the transducer and reflector held at each target temperature for more than 10 min before data acquisition to allow thermal stabilization. The excitation voltage, pulse width, and receiver gain were set to 200 V, 100 ns, and 35 dB, respectively. The echo signals were captured and digitized using a digital oscilloscope, and their fast Fourier transforms (FFTs) were calculated to determine the center frequency and -6 dB fractional bandwidth.

3. Results and discussion

3.1 Crystal structures and chemical states

Figure 1(a) shows the room-temperature X-ray diffraction (XRD) patterns of the CBN-KCS-100x ceramics. All samples exhibit diffraction patterns consistent with the orthorhombic $CaBi_2Nb_2O_9$ structure (PDF#49-0608), with no secondary phases detected within the resolution of the laboratory XRD measurements[34][37]. The most evident structural change occurs around the (200)/(020) doublet: the two peaks gradually approach each other and, at x = 0.14, merge almost completely into a single broad peak (Fig. 1(b) and Fig. S1, (Supplementary Material)). Rietveld refinements based on the orthorhombic $A2_1am$ model describe all compositions (Fig. S2). The refined lattice parameters (Fig. 1(c, d)) show that a and b converge, while c expands slightly. The orthorhombicity a/b decreases from 1.008 to 1.002, and the unit-cell volume increases by less than

Just Accepted

0.5%. Notably, even at x = 0.14 the merged doublet remains resolvable into two components and *a/b* stays above unity, indicating a pseudo-tetragonal metric with residual orthorhombic distortion rather than a true tetragonal phase. For bismuth layer-structured ferroelectrics, this convergence of the in-plane axes weakens the strong anisotropy that otherwise constrains polarization rotation and is therefore favorable for enhancing the macroscopic piezoelectric response[38][40]. The convergence of a and b reflects a reduction in the average in-plane lattice distortion following K/Ce/Sm co-substitution, while the accompanying changes in *c* and unit-cell volume indicate an adjustment of the Aurivillius lattice. The structural evolution is therefore characterized by increasingly similar in-plane lattice parameters within the retained orthorhombic framework.

XPS was used to examine the composition-dependent surface chemical states of the CBN-KCS-100*x* ceramics. The O1s spectra in Fig. 1(e) were fitted with a lattice-oxygen component and higher-binding-energy components associated with surface oxygen environments, including hydroxylated or adsorbed species and oxygen in modified local coordination environments[41]. The peak-area ratio labelled O_{HBE}/O_{LBE} in Fig. 1(e) decreases from 1.061 in undoped CBN to 0.857 at x = 0.10 and 0.563 at x = 0.12, before increasing to 1.433 at x = 0.14. This non-monotonic evolution identifies a composition-dependent redistribution of the surface oxygen spectral contributions, with the smallest relative higher-binding-energy contribution at x = 0.12. The complementary Ce3d spectra in Fig. S3(c) were analyzed using Ce^{3+} components (v_0, v', u_0, and u') and Ce^{4+} components (v, v'', v''', u, u'', and u''')[42]. The Ce3d fitting indicates the coexistence of Ce^{3+} and Ce^{4+}. Under the nominal Ca-site substitution model, with $f = Ce^{4+}/(Ce^{3+} + Ce^{4+})$, the average valence of the $(K_{0.5}Ce_{0.25}Sm_{0.25})$ substituent is $2 + 0.25f$, corresponding to a formal excess positive charge of $0.25f$ elementary charges per substituted Ca site, or $0.25xf$ per nominal formula unit. This residual donor character may modify the native charge-compensation balance and reduce the contribution of hole carriers to electrical conduction, thereby contributing to the increased resistivity. This charge-balance loop explains why ρ_{dc} increases most strongly at x = 0.12. The higher DC resistivity of CBN-KCS-12 relative to undoped CBN, discussed in Section 3.5, establishes the improvement in electrical insulation, whereas the stronger dielectric dispersion and higher loss at x = 0.14 indicate an increased dissipative response. Together with the XRD results, these observations identify x = 0.12 as a favorable balance between average lattice modification and electrical stability.

Just Accepted

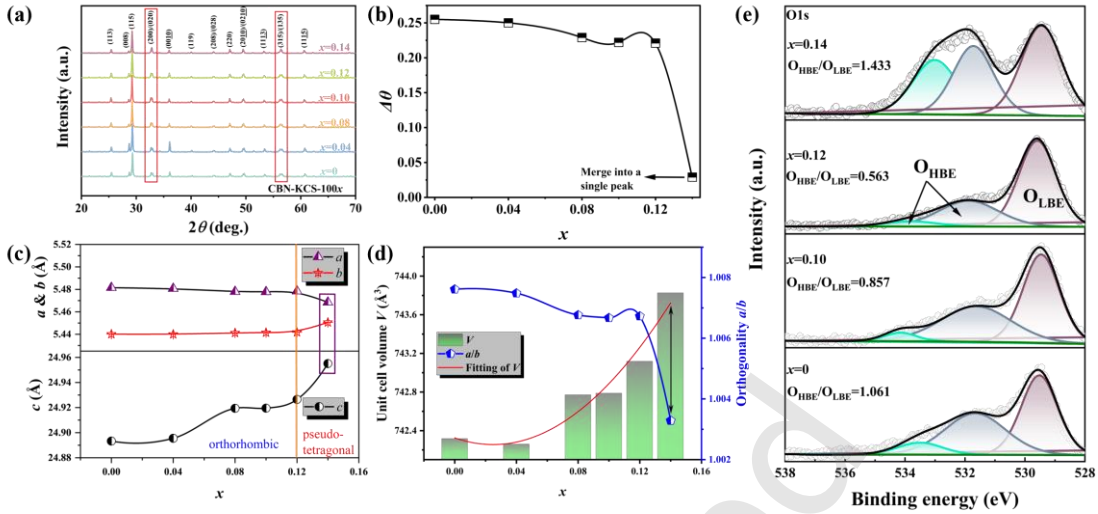


Fig. 1. Structural characterization and O1s XPS spectra of the CBN-KCS-100x ceramics: (a) room-temperature XRD patterns; (b) separation between the (200) and (020) diffraction peaks as a function of x; (c) lattice parameters a, b, and c; (d) unit-cell volume V and lattice-parameter ratio a/b; and (e) fitted O1s spectra for x = 0, 0.10, 0.12, and 0.14.

3.2 Microstructures and compositions

Scanning electron microscopy (SEM) images (Fig. S4) reveal well-defined plate-like grains in the CBN-KCS-100x ceramics, a typical microstructural feature of bismuth layer-structured ferroelectrics (BLSFs)[43][45]. The narrowest grain-size distribution is obtained at x = 0.12. Co-substitution suppresses grain growth along the longitudinal direction and reduces the grain aspect ratio, an evolution consistent with the pseudo-tetragonal distortion observed by XRD. Energy-dispersive X-ray spectroscopy (EDS) mapping of the x = 0.12 sample shows relatively uniform distributions of Ca, Bi, Nb, O, K, Ce, and Sm within the examined region, with no obvious elemental segregation at the spatial resolution of the measurement.

3.3 Dielectric properties

$K^+/Ce^{4+}/Sm^{3+}$ co-substitution modifies the dielectric response while retaining the high transition temperature of CBN. The dielectric maxima measured at 1 MHz identify the ferroelectric-paraelectric transition and determine T_C[46]. The overall decrease in T_C is consistent with the reduced orthorhombic distortion identified by XRD, while CBN-KCS-12 retains a T_C of approximately 933 °C (Fig. 2(a, b)). The room-temperature dielectric loss initially decreases and then rises with substitution content, indicating that the reduction in dielectric dissipation is limited to an appropriate compositional range.

The diffuseness of the dielectric transition was evaluated using the modified Curie-Weiss

Just Accepted

law[47][48]:

$$\frac{1}{\varepsilon_r} - \frac{1}{\varepsilon_m} = \frac{(T-T_m)^\gamma}{C} \quad (1)$$

where ε_m is the maximum relative permittivity at T_m, C is the fitted Curie-like constant, and γ is the diffuseness exponent. Values of γ approaching 1 and 2 correspond to a sharp Curie-Weiss-type transition and a strongly diffuse transition, respectively[49]. The overall increase in γ indicates a more diffuse dielectric transition, consistent with the chemical disorder introduced by A-site substitution, which can create spatial variations in the local polarization environment. A connection between disorder and heterogeneous polar responses has also been discussed theoretically by Bishop et al[50]. The increase in γ indicates a more diffuse transition, consistent with the chemical disorder introduced by A-site substitution. Meanwhile, C increases overall with some compositional fluctuations, reflecting changes in the dielectric response above T_m.

The room-temperature frequency response provides a complementary measure of dielectric stability (Fig. 2(c, d)). The decrease in ε_r with increasing frequency is consistent with a diminishing contribution from slower polarization processes, including space-charge and interfacial polarization. The relative permittivity variation was quantified as[51]:

$$\eta = \frac{\varepsilon_r(f_0) - \varepsilon_r(f)}{\varepsilon_r(f_0)} \quad (2)$$

where f_0 = 100 Hz and $\varepsilon_r(f_0)$ and $\varepsilon_r(f)$ are the relative permittivities at the reference and measurement frequencies, respectively. At 1 MHz, η decreases from 3.70% in undoped CBN to a minimum of 1.64% at x = 0.10, before rising to 7.05% at x = 0.14. Moderate co-substitution improves dielectric-frequency stability, whereas the stronger dispersion and elevated low-frequency loss at x = 0.14 are consistent with increased contributions from slow space-charge and interfacial polarization processes.

Just Accepted

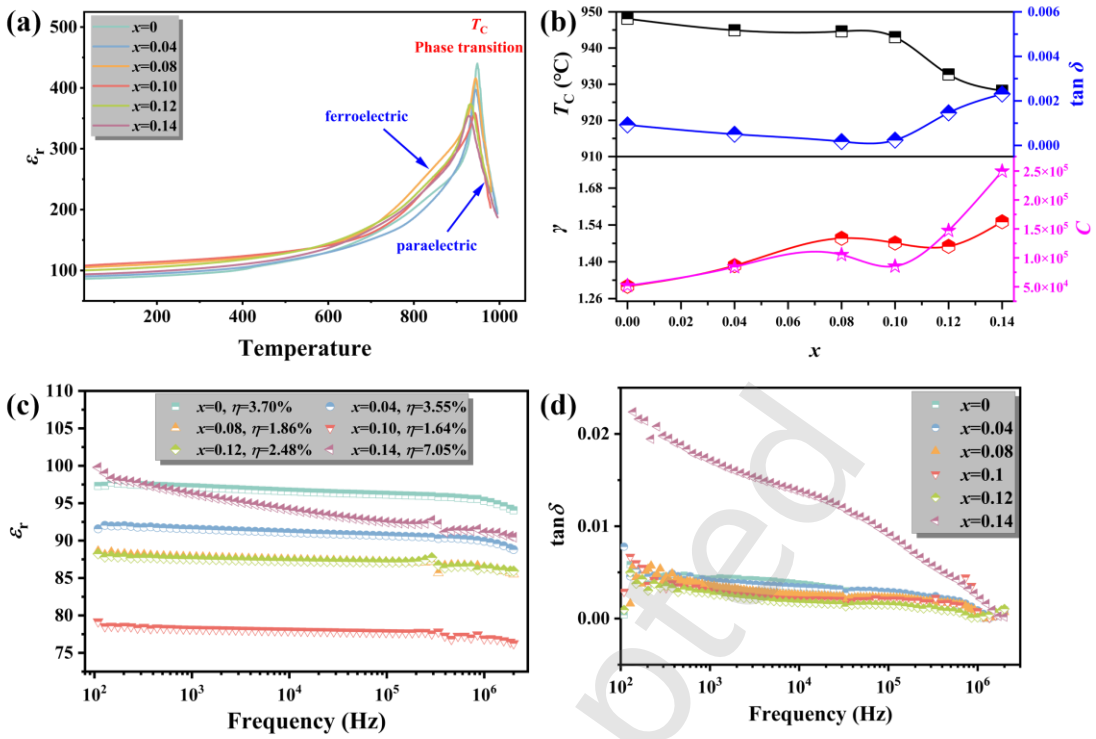


Fig. 2. Dielectric properties of the CBN-KCS-100x ceramics: (a) temperature dependence of the relative permittivity ε_r measured at 1 MHz; (b) Curie temperature T_C, room-temperature dielectric loss tanδ, and modified Curie-Weiss fitting parameters γ and C as functions of x; and room-temperature frequency dependence of (c) ε_r and (d) tanδ. The relative permittivity variations η between 100 Hz and 1 MHz are indicated in (c).

3.4 AC impedance and modulus

The electrical response of CBN-KCS-12 involves thermally activated conduction and distributed relaxation. To distinguish the grain and grain-boundary contributions, the impedance spectra were fitted using two series-connected parallel R-CPE elements (Fig. 3(a, b)). This model accounts for the non-ideal capacitive response associated with the depressed impedance arcs. The complex impedance is expressed as:

$$Z^* = \frac{R_g}{[1+R_g T_1(i\omega)^{n1}]} + \frac{R_{gb}}{[1+R_{gb} T_2(i\omega)^{n2}]} \quad (3)$$

where R_g and R_{gb} represent the grain and grain-boundary resistances, T_1 and T_2 are the constant-phase-element coefficients, and n_1 and n_2 characterize departures from ideal capacitive behavior. At 650 °C, n_1 = 0.9695 and n_2 = 0.8305 indicate that the grain response is closer to ideal Debye relaxation, whereas the grain-boundary response exhibits a broader relaxation-time distribution. Both resistances decrease with temperature, yielding activation energies of 1.35 and 1.31 eV, respectively (Fig. 3(c)). Their similar values indicate comparable thermal barriers for grain and

Just Accepted

grain-boundary transport.

The frequency-dependent impedance provides further information on conduction and relaxation, with its complex form written as[52]:

$$Z=Z'-jZ'' \tag{4}$$

where Z' and Z'' denote the resistive and loss components, respectively. The decrease in low-frequency Z' with temperature is consistent with thermally enhanced conduction. Meanwhile, the Z'' relaxation peak shifts toward higher frequencies, indicating a shorter characteristic relaxation time (Fig. 3(d, e))[53]. The relaxation is thermally activated, with an activation energy close to that of DC conduction (Section 3.5).

Impedance and modulus representations emphasize high-resistance and low-capacitance contributions, respectively, while modulus analysis reduces the influence of electrode polarization[54][55]. The complex modulus is defined as[56]:

$$M=M'+jM''=j\omega C_0 Z \tag{5}$$

where $C_0 = \varepsilon_0 A/d$ is the vacuum capacitance, and A and d are the electrode area and sample thickness. The modulus dispersion shifts toward higher frequencies with increasing temperature, consistent with the acceleration of relaxation observed in the impedance spectra (Fig. 3(f, g)). The broad, asymmetric M'' peaks indicate that the response cannot be described by a single relaxation time. Thus, heating changes both the characteristic relaxation rate and the distribution of relaxation times.

To evaluate this distribution, the peak-height-normalized spectra are compared in Fig. 3(h), and the M″ response is analyzed using the Bergman equation[57]:

$$M''(\omega)=\frac{M''_{max}}{1-\beta+\frac{\beta}{1+\beta}\left[\beta(\omega_{max}/\omega)+(\omega/\omega_{max})\right]^{\beta}} \tag{6}$$

where ω_{max} corresponds to M''_{max}, and β describes the departure from Debye relaxation ($\beta = 1$). The fitted β decreases slightly up to approximately 500 °C and subsequently increases, remaining below unity throughout the measured range (Fig. 3(i)). This evolution indicates initial broadening followed by narrowing of the relaxation-time distribution. The high-temperature response therefore approaches Debye behavior while retaining a distributed relaxation character.

Just Accepted

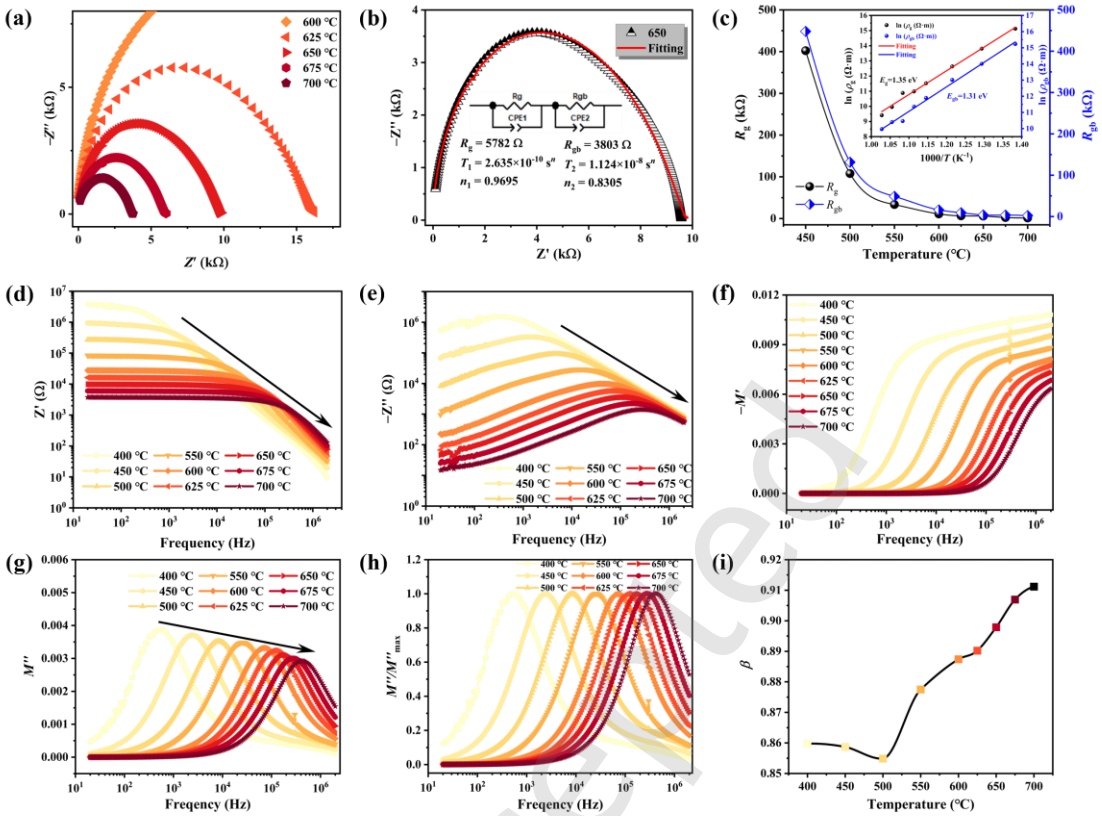


Fig. 3. Impedance and electric modulus spectra of CBN-KCS-12: (a) Nyquist plots measured from 600 to 700 °C; (b) experimental and fitted Nyquist plots at 650 °C, with the equivalent circuit and fitted parameters; (c) temperature dependence of the fitted resistances R_g and R_{gb}, with the corresponding Arrhenius plots in the inset; frequency dependence of (d) Z', (e) $-Z''$, (f) M', (g) M'', and (h) normalized M''/M''max at different temperatures; and (i) temperature dependence of the parameter β obtained from Bergman fitting.

3.5 Electrical conduction behaviors

Figure 4(a-d) presents the frequency- and temperature-dependent electrical response of CBN-KCS-12. The conductivity increases with temperature and exhibits a nearly frequency-independent plateau at low frequencies, followed by a dispersive contribution at higher frequencies. The plateau represents the DC contribution, whereas the dispersive region reflects charge dynamics on shorter time scales. The conductivity spectra can be described by Jonscher's power law[58]:

$$\sigma(\omega)=\sigma_{dc}(T)+A\omega^{n} \quad (7)$$

Here, σ_{dc} is the frequency-independent conductivity, A is a temperature-dependent coefficient, ω is the angular frequency, and n is the frequency exponent. As shown in Fig. 4(b, c), n decreases from 0.642 at 400 °C to 0.109 at 700 °C. This trend is qualitatively consistent with thermally assisted hopping described by the correlated barrier-hopping model[59]. The more pronounced decrease

Just Accepted

between 500 and 600 ℃ indicates a change in the temperature dependence of the dispersive response. Together with the impedance and modulus results, this behavior reflects the evolution of thermally activated charge dynamics. The crossover between the DC plateau and the dispersive contribution can be characterized by ω_p, defined by $A\omega_p n = \sigma_{dc}$[60]:

$$\omega_p=(\frac{\sigma_{dc}}{A})^{1/n} \quad (8)$$

Its temperature dependence can be expressed using an Arrhenius relation:

$$\omega_p=\omega_0 \exp(-E_p/K_B T) \quad (9)$$

where ω_0 is the prefactor and E_p is the apparent activation energy associated with the characteristic frequency. The increase in ω_p with temperature shown in Fig. 4(d) describes an acceleration of the electrical response. In this analysis, ω_p characterizes the crossover between frequency-independent and dispersive conduction.

Figure 4(e) compares the DC resistivities of undoped CBN and CBN-KCS-12. Both compositions exhibit decreasing resistivity with increasing temperature, while CBN-KCS-12 maintains a higher resistivity throughout the measured range. At 650 ℃, the resistivity increases from 1.40×10^5 Ω·cm in undoped CBN to 2.59×10^6 Ω·cm in CBN-KCS-12, corresponding to an approximately 18.5-fold increase. The Arrhenius fits over 400-700 ℃ yield apparent conduction activation energies of approximately 1.0 and 1.1 eV, respectively (Fig. 4(f)). These results establish improved high-temperature electrical insulation and a modest increase in the effective thermal barrier for DC conduction following co-substitution.

Previous studies have reported predominantly hole conduction in undoped CBN and increased resistivity upon moderate donor substitution[61]. Within the partial donor-acceptor compensation model discussed in Section 3.1, the residual donor character of K/Ce/Sm co-substitution provides a plausible route for reducing the contribution of native hole carriers. Changes in defect mobility and grain-boundary transport may also contribute to the measured resistivity. The improved insulation is therefore attributed to charge compensation and a reduced hole concentration.

Just Accepted

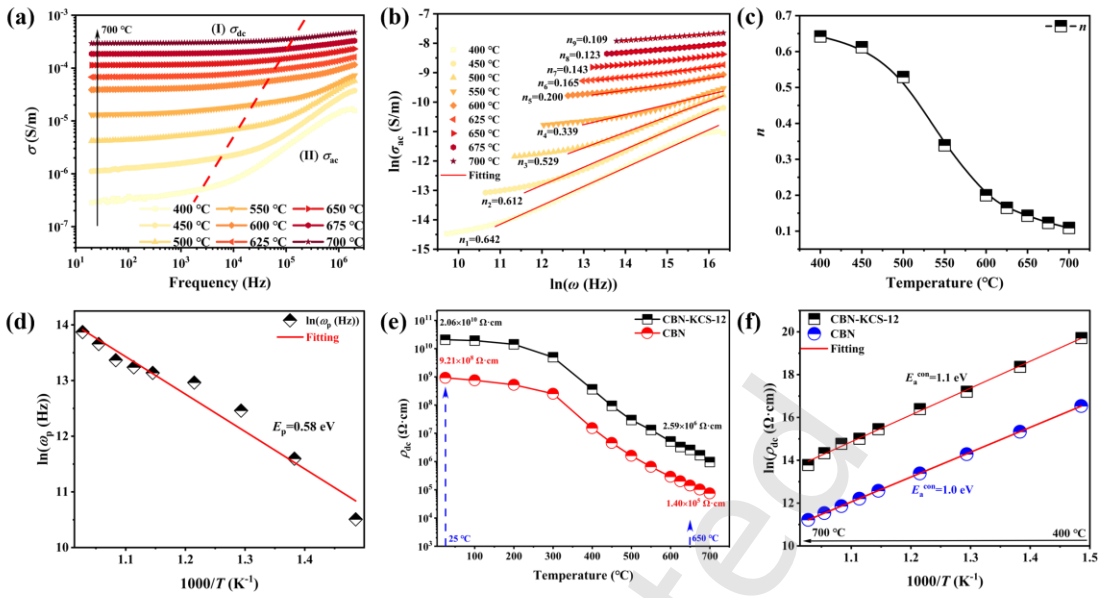


Fig. 4. Electrical conductivity of CBN-KCS-12 and DC resistivity comparison with undoped CBN: (a) conductivity spectra at different temperatures; (b) logarithmic conductivity-angular-frequency plots and fitted curves; (c) temperature dependence of the frequency exponent n; (d) Arrhenius plot of the crossover angular frequency ω_p; (e) temperature-dependent DC resistivity ρ_{dc} of undoped CBN and CBN-KCS-12; and (f) corresponding plots of $\ln\rho_{dc}$ versus $1000/T$ with linear fits over 400-700 °C.

3.6 Electromechanical coupling properties

To systematically investigate the electromechanical energy coupling behavior of piezoelectric ceramics, the planar radial resonance spectra of the CBN-KCS-100x ceramics were measured between 295 kHz and 320 kHz. As shown in Fig. 5(a), the phase angle θ of all compositions increases from -90° to a maximum within the resonance-antiresonance interval (f_r-f_a) at room temperature. Theoretically, under ideal poling conditions, the maximum phase angle θ_{max} should approach 90°. However, due to the inherent difficulty in polarizing bismuth layer-structured ferroelectrics, ideal polarization is generally not achieved, and this limitation also applies to the CBN-KCS-100x ceramics.

Both θ_{max} and the resonance bandwidth (f_r-f_a) increase gradually with doping concentration. Among the CBN-KCS-100x ceramics, CBN-KCS-12 exhibits a peak θ_{max} of 78.4° and a broadened resonance bandwidth of 0.70 kHz, suggesting that doping facilitates ferroelectric-domain switching and creates favorable conditions for sufficient polarization. The simultaneous enhancement of θ_{max} and the bandwidth improves polarizability and implies a broader frequency response and higher output voltage under high-frequency excitation, laying a solid performance foundation for high-temperature ultrasonic transducer applications. Fig. 5(b) shows k_p and Q_m of the CBN-KCS-100x ceramics versus x: CBN-KCS-12 achieves the largest electromechanical coupling factor (k_p = 6.97%) and mechanical quality factor (Q_m = 2800), indicating both efficient energy conversion and low mechanical loss.

Just Accepted

Figure 5(c, d) shows the temperature-dependent resonance behavior of CBN-KCS-12. With increasing temperature, the resonance frequency initially decreases from approximately 310 to 302 kHz. Above 500 ℃, it shifts to approximately 307 kHz and then decreases to about 305 kHz. Meanwhile, the impedance peak becomes less pronounced, and the maximum phase angle decreases overall, showing that the resonance response weakens with heating.

The weakening of the resonance response accompanies the increase in conductivity shown in Fig. 4. At elevated temperatures, enhanced charge transport increases electrical loss and affects the measured impedance response. The frequency change near 500 ℃ occurs in the temperature range where the conductivity dispersion and electrical relaxation also change. These results suggest that thermally activated charge transport and relaxation may contribute to the observed shift of the impedance peak.

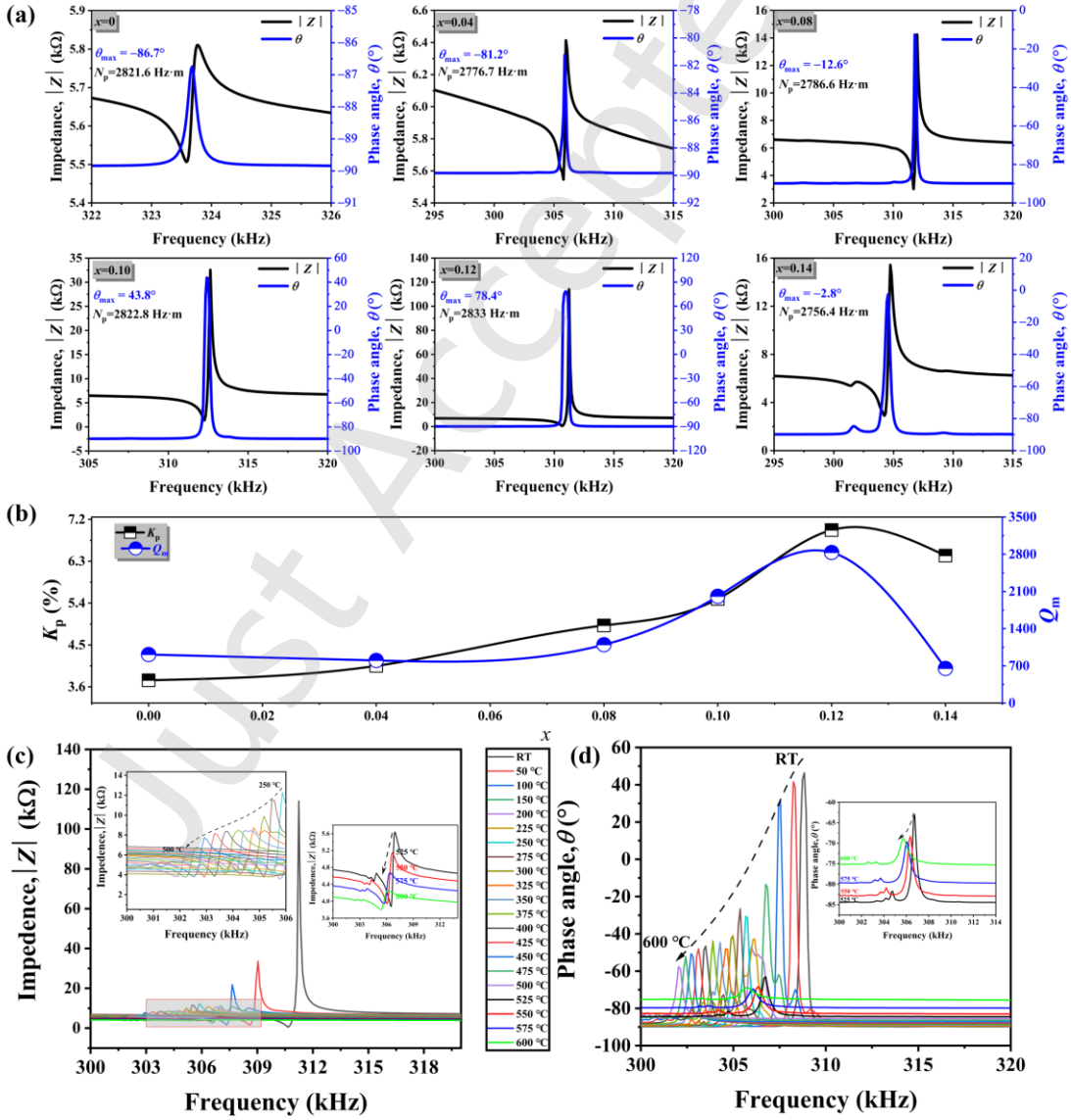


Fig. 5. Electromechanical resonance characteristics of the CBN-KCS-100x ceramics: (a) room-temperature impedance magnitude $|Z|$ and phase angle θ near the planar radial resonance, with the maximum phase angle θ_{max}

Just Accepted

and planar frequency constant N_p indicated; (b) planar electromechanical coupling factor k_p and mechanical quality factor Q_m as functions of x; and frequency dependence of (c) $|Z|$ and (d) θ for CBN-KCS-12 at temperatures from room temperature to 600 °C. The insets in (c) and (d) show enlarged portions of the spectra.

3.7 Piezoelectric properties and thermal depolarization behavior

Figure 6(a) shows the room-temperature piezoelectric coefficient d_{33} and voltage coefficient g_{33} of the CBN-KCS-100x ceramics, where $g_{33} = d_{33}/(\varepsilon_0\varepsilon_r)$[62]. Both coefficients reach their maxima at x = 0.12, with d_{33} increasing from approximately 5 pC/N in undoped CBN to 18 pC/N. As the lattice parameters a and b become closer, the reduced in-plane distortion can facilitate polarization switching under an applied electric field, allowing more domains to align during poling. This interpretation agrees with the improved electromechanical coupling in Fig. 5 and previous studies of CBN-based ceramics. At x = 0.14, d_{33} decreases despite the continued convergence of a and b. The simultaneous increase in dielectric dispersion, tanδ, and the surface oxygen ratio indicates that the useful substitution range is limited by defect-related disorder and space-charge effects, which reduce the switchable polarization and the poling efficiency. The optimum at x = 0.12 therefore reflects a defect/kinetic limit rather than a phase boundary.

Thermal stability was evaluated by measuring d_{33} at room temperature after annealing at different temperatures (Fig. 6(b)). Here, the depolarization temperature T_d is defined as the annealing temperature at which d_{33} falls to 50% of its initial value. T_d increases from 600 °C in undoped CBN to 850 °C in CBN-KCS-12, which retains approximately 44% of its initial d_{33} after annealing at 900 °C. These results demonstrate improved resistance to thermal depolarization. The Curie temperature T_C, approximately 933 °C for CBN-KCS-12, marks the ferroelectric-paraelectric transition, whereas T_d describes the decrease in piezoelectric performance after heating. The difference between these temperatures reflects the partial loss of the polarization alignment established during poling before the ceramic reaches T_C.

Figure 6(c-f) compares the room-temperature PFM images before and after annealing at 900 °C. Before annealing, undoped CBN shows fine stripe-like patterns, whereas CBN-KCS-12 exhibits larger block-like regions. After annealing and natural cooling without repoling, the stripe-like pattern in undoped CBN becomes more fragmented, while block-like regions remain visible in CBN-KCS-12. Similar differences are observed in the in-plane PFM images in Fig. S5. The persistence of the block-like pattern, together with the higher retained d_{33}, suggests that the domain arrangement in CBN-KCS-12 is less affected by the heat treatment.

The enhanced piezoelectric response and thermal stability are associated with improved polarization alignment during poling and better preservation of this alignment during heating. The reduced lattice distortion can facilitate polarization switching under the applied electric field, contributing to the higher d_{33}. Meanwhile, the higher d_{33} retention after annealing, together with the observed domain morphology, suggests that co-substitution helps limit the loss of polarization alignment during heating.

Just Accepted

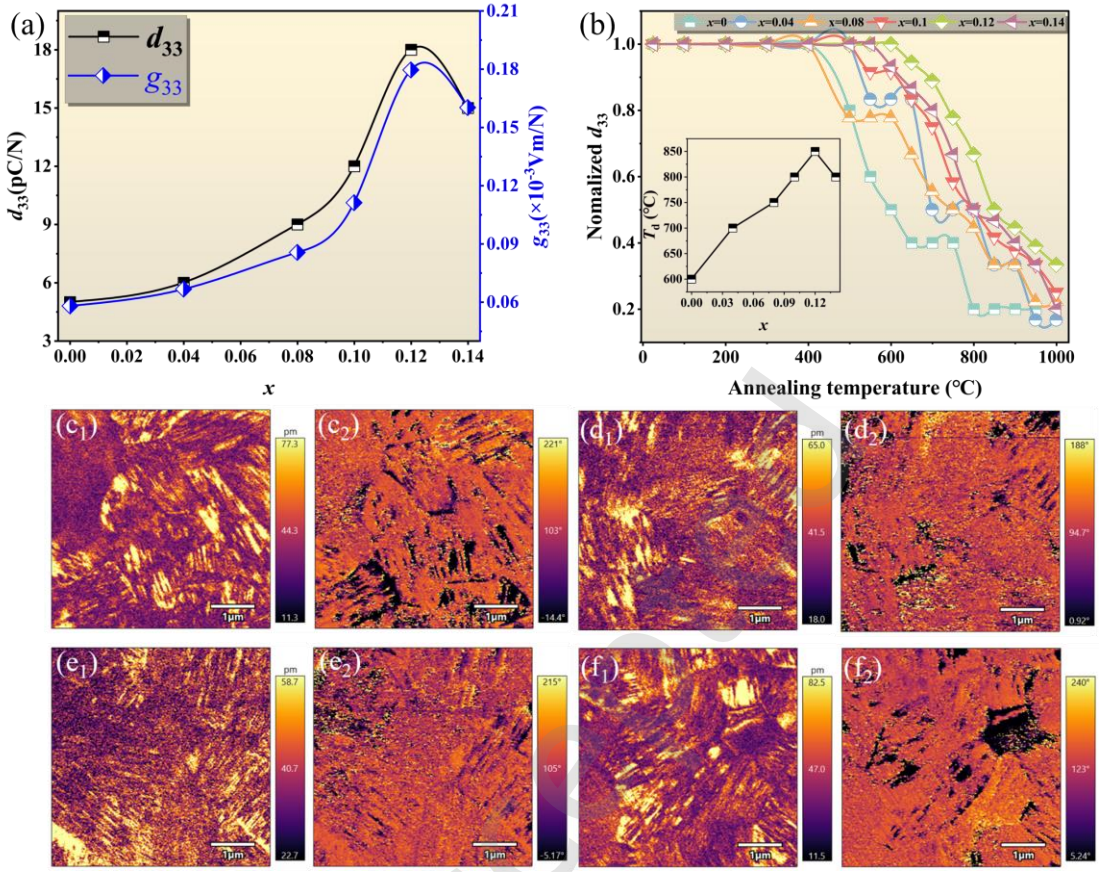


Fig. 6. Piezoelectric properties and PFM images of the CBN-KCS-100x ceramics: (a) room-temperature piezoelectric coefficient d_{33} and voltage coefficient g_{33} as functions of x; (b) normalized d_{33} measured at room temperature after annealing at different temperatures, with the inset showing the depolarization temperature T_d defined by 50% retention of the initial d_{33}; and out-of-plane PFM amplitude and phase images of (c_1, c_2) undoped CBN before annealing, (d_1, d_2) CBN-KCS-12 before annealing, (e_1, e_2) undoped CBN after annealing, and (f_1, f_2) CBN-KCS-12 after annealing. Subscripts 1 and 2 denote amplitude and phase images, respectively. For the post-annealing PFM measurements, the samples were annealed at 900 °C for 2 h in air and naturally cooled to room temperature without repoling. All PFM scale bars represent 1 μm.

3.8 Mechanical properties

Figure 7(a, b) shows the nanoindentation load-depth curves of undoped CBN and CBN-KCS-12 under peak loads of 10-50 mN. In both compositions, the loading and unloading branches form a closed hysteresis loop, with a residual depth hp remaining after unloading that reflects irreversible deformation. Under the same peak load, CBN-KCS-12 exhibits slightly smaller maximum indentation depths h_m and residual depths h_p at all tested loads (Fig. 7(c)), indicating improved indentation resistance and a larger elastic recovery fraction.

Just Accepted

Figure 7(d) compares the compressive stress-strain responses of pure CBN and CBN-KCS-12. Under the same applied stress, CBN-KCS-12 exhibits a smaller strain, with the measured modulus increasing from 30.1 to 33.8 GPa. This increase in stiffness may involve combined changes in grain-scale mechanical constraints, lattice elasticity, and ferroelastic domain responses. As shown in Fig. S4, the average lengths of the plate-like grains in pure CBN and CBN-KCS-12 are approximately 9.8 and 3.4 μm, respectively, while the average thickness is approximately 0.95 μm for both compositions. Grain boundaries can influence domain behavior in ferroelectric ceramics[63]. The smaller grain size in CBN-KCS-12 may therefore also affect its deformation under compression. Meanwhile, the changes in lattice parameters and orthorhombic distortion indicate that co-substitution modifies the crystal structure and may influence the intrinsic elastic response through changes in local coordination and bonding[64].

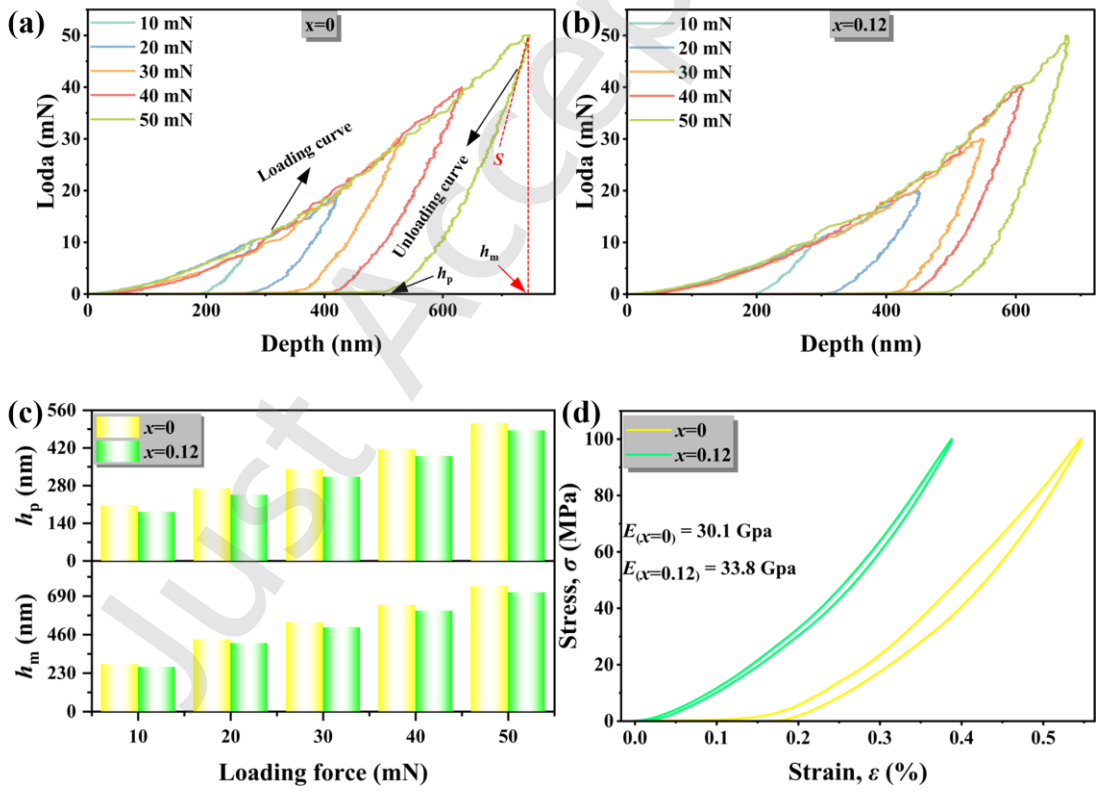


Fig. 7. Mechanical properties of CBN and CBN-KCS-12 ceramics: (a, b) nanoindentation load-depth curves of CBN and CBN-KCS-12 ceramics, respectively, under loads of 10-50 mN; (c) maximum indentation depth h_m and residual indentation depth h_p under different loads; (d) compressive stress-strain curves measured up to 100 MPa, with the inset showing the corresponding elastic moduli.

3.9 High-temperature ultrasonic transducer performance

Just Accepted

Figure S6 shows the assembled CBN-KCS-12 transducer (Fig. S6(a)), its layer configuration (Fig. S6(b)), and the high-temperature pulse-echo measurement system (Fig. S6(c)). The device consists of a CBN-KCS-12 element with fired silver electrodes, a quarter-wave epoxy/alumina matching layer, an epoxy/tungsten backing layer, and a cylindrical brass housing. The measurement system comprises a pulser/receiver, a digital oscilloscope, and a muffle furnace, in which the transducer and an alumina ceramic reflector are mounted. The pulse-echo response was recorded from room temperature to 400 ℃, as detailed in Section 2.3.

The pulse-echo response of this device was measured from room temperature to 400 ℃ (Fig. 8(a) and Fig. S7). At 400 ℃, the transducer still delivers a well-defined echo, with a signal-to-noise ratio above 36 dB and a -6 dB fractional bandwidth of approximately 42%.

As summarized in Fig. 8(b), the center frequency shifts only slightly and the -6 dB bandwidth narrows modestly over the whole range, indicating that the fundamental vibration mode and acoustic resonance remain intact. In contrast, the peak-to-peak voltage and signal energy decrease progressively while the insertion loss rises; insertion loss and signal energy maintain an approximately inverse correlation (Fig. 8(c)). Temperature therefore weakens the acoustic-energy transfer efficiency rather than shifting or destabilizing the operating mode.

Given the high T_C (933 ℃), the high DC resistivity at 650 ℃, and the thermally stable block-domain configuration established above, this amplitude attenuation is unlikely to come from depolarization or failure of the CBN-KCS-12 element itself. It is more likely caused by the matching layer, backing layer, and dry-contact interface, whose acoustic properties and thermal expansion change with temperature and increase interface dissipation. The transducer therefore shows that CBN-KCS-12 still provides usable pulse-echo output at 400 ℃, and the remaining signal loss arises from the device assembly rather than the ceramic.

Just Accepted

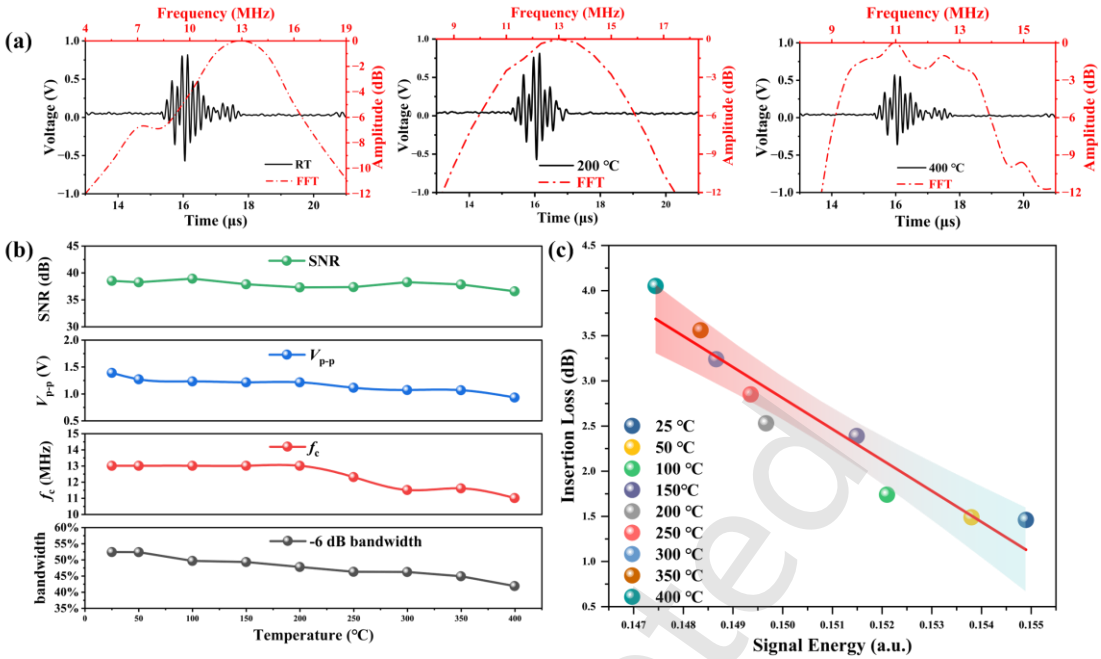


Fig. 8. Temperature-dependent responses of the CBN-KCS-12-based ultrasonic transducer: (a) pulse-echo waveforms and corresponding FFT spectra at room temperature, 200 °C, and 400 °C; (b) SNR, peak-to-peak echo voltage, center frequency, and -6 dB fractional bandwidth as functions of temperature; (c) relationship between insertion loss and signal energy at different temperatures.

4. Conclusions

This work investigated a multi-element A-site co-substitution strategy for improving the piezoelectric activity and thermal stability of Aurivillius-type $CaBi_2Nb_2O_9$ ceramics through K/Ce/Sm substitution at the Ca site. The optimized CBN-KCS-12 ceramic exhibited d_{33} = 18 pC/N and $T_C \approx 933$ °C. Its ρ_{dc} resistivity at 650 °C reached 2.59 × 10^6 Ω·cm, approximately 18.5 times that of undoped CBN. The depolarization temperature, defined by 50% retention of the initial d_{33} after annealing, increased from 600 to 850 °C, and approximately 44% of the initial d_{33} remained after annealing at 900 °C. The measured elastic modulus increased from 30.1 to 33.8 GPa.

The enhanced piezoelectricity, high-temperature insulation, and thermal depolarization resistance arose from the synergistic effects of charge compensation and structural evolution. The residual donor character of the K/Ce/Sm substituent reduced the contribution of native hole carriers through partial donor-acceptor compensation, thereby preserving high-temperature electrical insulation. Meanwhile, the K/Ce/Sm co-substitution drove the in-plane lattice parameters to converge toward a pseudo-tetragonal metric within the retained orthorhombic framework and

Just Accepted

transformed fine stripe domains into larger block-like regions, improving polarization alignment during poling and its retention after thermal exposure.

At the device level, a single-element ultrasonic transducer fabricated from CBN-KCS-12 delivered a clear pulse-echo signal at 400 ℃ with a signal-to-noise ratio above 36 dB and a -6 dB bandwidth of approximately 42%. The echo remained recognizable across the entire measured range from room temperature to 400 ℃, with the center frequency shifting only modestly, confirming that the active ceramic remained electromechanically functional up to the operating temperature. By coupling multi-element defect engineering with block-domain stabilization, this work establishes a composition design principle for Aurivillius piezoceramics that simultaneously addresses piezoelectric activity, high-temperature resistivity, thermal depolarization stability, and mechanical stiffness, providing a material-to-device pathway for ultrahigh-temperature ultrasonic sensing up to 400 ℃.

Availability of data and materials

The data that support the findings of this study are available from the corresponding author upon reasonable request.

Conflict of interest

The authors declare that they have no conflict of interest.

Acknowledgments

This work was funded by the National Natural Science Foundation of China (Grant No. 12372179, 12602109) and the "Hundred-Person" Talent Program of Xihua University (Grant No. T2026086).

Electronic Supplementary Material

Supplementary material (deconvolution of the (200)/(020) reflections in Fig. S1; Rietveld refinement profiles in Fig. S2; XPS survey, Ca2p, and Ce3d spectra in Fig. S3; SEM images, grain-size distributions, and EDS analysis in Fig. S4; AFM topography and in-plane PFM images before and after annealing in Fig. S5; photographs and a structural schematic of the ultrasonic transducer

Just Accepted

and its measurement setup in Fig. S6; and additional pulse-echo waveforms and FFT spectra in Fig. S7) is available in the online version of this article.

References

[1] O'Malley CJ, Tang X, Koval V, et al. Unveiling the mechanism of substitution-induced high piezoelectric performance in PLZT ceramics. J. Adv. Ceram. 2025, 14: 9221097.

[2] Yang A, Huan Y, Wang Q, et al. Excellent comprehensive piezoelectric performances of SiC-doped BCTZ-based lead-free piezoelectric ceramics. J. Adv. Ceram. 2025, 14: 9221054.

[3] Chen Y, Zhou Z, Li L, et al. Synergistically enhancing the piezoelectric activity and Curie temperature of CaBi4Ti4O15 ceramics via co-doping Gd/Mn at the A/B-site. J. Adv. Ceram. 2024, 13: 1482-1497.

[4] Liu H, Hao Y, Yang Z, et al. Exceptional electrostrain with minimal hysteresis and superior temperature stability under low electric field in KNN-based lead-free piezoceramics. J. Adv. Ceram. 2024, 13: 364-372.

[5] Yin Y, Wu W, Zhang S, et al. Simultaneous enhancement of piezoelectric coefficient and depolarization temperature in BF-BT-based ceramics via heterogeneous structure design. J. Adv. Dielectr. 2026: 2650020.

[6] Chen L, Wu Y, Ul Hasnain Bakhtiar S, et al. Synergetic enhancement of electric polarization and magnetization in Fe-doped Pb(Zr0.52Ti0.48)O3 modulated with “magnetoelectric composite” defect-dipoles. J. Adv. Dielectr. 2025, 15: 2550001.

[7] Li Y X, Fan H Q, Chen H, et al. Performance enhancement and structural defect chemistry regulation of Bi_3TiNbO_9 high-temperature piezoelectric ceramics by (W, Mn) co-doping. Ceram. Int. 2026, 52(21): 38434–38444.

[8] Luo B, Feng W, Dai S, et al. Stabilizing oxygen vacancies and promoting electrostrain in lead-free potassium niobate-based piezoelectrics over wide temperature ranges. J. Adv. Ceram. 2024, 13: 1965-1973.

[9] Chen XY, Li B, Dai YJ, et al. Enhanced high-temperature piezoelectric performance of Bi4Ti3O12-based ceramics via multi-element co-doping and domain engineering. Rare Met. 2025, 44: 6575-6584.

[10] Xu J, Xie S, Xu Q, et al. Significantly enhanced performance and conductivity mechanism in

Just Accepted

Nb/Mn co-doped CaBi4Ti4O15 ferroelectrics. J. Materiomics 2024, 10: 652-669.

[11] Ren J, Liu Q, Cai E, et al. Synergistically enhanced electrical properties in BCST lead-free piezoelectric ceramics via defect-driven lattice distortion within the polymorphic phase boundary. J. Adv. Dielectr. 2026: 2650009.

[12] Li A, Bin C, Hou X, et al. Machine learning-assisted design of CaBi2Nb2O9-based ceramics with high piezoelectricity and thermal stability. Ceram. Int. 2025, 54: 4750-4756.

[13] Damjanovic D. Materials for high temperature piezoelectric transducers. Curr. Opin. Solid State Mater. Sci. 1998, 3: 469-473.

[14] Wen Q, Guo HH, Shen ZY, et al. MnO2 doping induced structural tuning drives superior piezoelectric response in CaBi4Ti4O15-based ceramics. J. Adv. Ceram. 2025, 14: 9221051.

[15] Yan HX, Zhang HT, Ubic R, et al. A lead-free high-Curie-point ferroelectric ceramic, CaBi2Nb2O9. Adv. Mater. 2005, 17: 1261-1265.

[16] Yan Y, Qiao Y, Wang L, et al. A novel strategy for obtaining lead-based piezoelectric ceramics with giant piezoelectricity and high-temperature stability through the construction of "slush-like" polar states. J. Mater. Sci. Technol. 2025, 221: 25-35.

[17] Liu Q, Liang D, Xiong J, et al. Bi2WO6/spontaneously polarized ceramic-g-C3N4 heterojunction with dynamic cascade electric fields to deplete unilaterally accumulated charges and break carrier shielding effect for boosting piezo-photocatalysis. J. Mater. Sci. Technol. 2025, 230: 93-105.

[18] Huang J, Li J, Li M, et al. Chemical composition regulation to enhance the energy storage property of the lead-free relaxor ferroelectric. J. Adv. Ceram. 2026, 15: 9221298.

[19] Zhang H, Wang B, Wang J, et al. Defect dipole gradient design in (K, Na) NbO3-based piezoelectric ceramics enabling controllable ultrahigh bending deformation. J. Mater. Sci. Technol. 2025, 239: 234-242.

[20] Long C B, Fan H Q, Ren P R. Structure, phase transition behaviors and electrical properties of Nd substituted Aurivillius polycrystallines $Na_{0.5}Nd_xBi_{2.5-x}Nb_2O_9$ (x = 0.1, 0.2, 0.3, and 0.5). Inorg. Chem. 2013, 52(9): 5045–5054.

[21] Qiu C, Wang Y, Jin R, et al. Achieving high piezoelectric performance and enhanced high-temperature resistivity in CaBi2Nb2O9-based textured ceramics. J. Am. Ceram. Soc. 2025, 108: e20587.

Just Accepted

[22] Chen Z, Sheng L, Li X, et al. Enhanced piezoelectric properties and electrical resistivity in W/Cr co-doped CaBi2Nb2O9 high-temperature piezoelectric ceramics. Ceram. Int. 2019, 45: 6004-6011.

[23] Long C, Ren W, Zheng K, et al. Ultrahigh-temperature piezoelectric polycrystalline ceramics: dramatically enhanced ferroelectricity, piezoelectricity and electrical resistivity in Ca1-3xBi2+3x Nb2-xMnxO9. Mater. Res. Lett. 2020, 8: 165-172.

[24] Chen Z, Zhang Y, Huang P, et al. Enhanced piezoelectric properties and thermal stability in Mo/Cr co-doped CaBi2Nb2O9 high-temperature piezoelectric ceramics. J. Phys. Chem. Solids 2020, 136: 109195.

[25] Chen H, Zhai J. Enhancing piezoelectric performance of CaBi2Nb2O9 ceramics through microstructure control. J. Electron. Mater. 2012, 41: 2238-2242.

[26] Long C, Wang B, Ren W, et al. Significantly enhanced electrical properties in CaBi2Nb2O9-based high-temperature piezoelectric ceramics. Appl. Phys. Lett. 2020, 117: 032902.

[27] Hou D W, Fan H Q, Zhang A, et al. Role of BO_6 octahedral distortion on high temperature piezoelectric properties in $Bi_{3-x}(Li_{0.5}Sm_{0.5})_xTiNbO_9$. Ceram. Int. 2022, 48(15): 22163–22171.

[28] Chen X, Ou B, Liu G, et al. Simultaneous enhancement of piezoelectric performance and Curie temperature in high-temperature Bi4Ti3O12 piezoceramics through A/B site co-doping. J. Adv. Ceram. 2025, 14: 9221077.

[29] Tian X, Qu S, Du H, et al. Effects of (LiCe) co-substitution on the structural and electrical properties of CaBi2Nb2O9 ceramics. Chin. Phys. B 2012, 21: 037701.

[30] Wang C, Zhang S, Wang J, et al. Electromechanical properties of calcium bismuth niobate (CaBi2Nb2O9) ceramics at elevated temperature. Mater. Chem. Phys. 2009, 118: 21-24.

[31] Wang C, Wang J, Zhang S, et al. Piezoelectric and electromechanical properties of ultrahigh temperature CaBi2Nb2O9 ceramics. Phys. Status Solidi RRL 2009, 3: 2-3.

[32] Liu G, Wang D, Wu C, et al. A realization of excellent piezoelectricity and good thermal stability in CaBi2Nb2O9: pseudo phase boundary. J. Am. Ceram. Soc. 2019, 102: 1794-1804.

[33] Onoe M, Jumonji H. Useful formulas for piezoelectric ceramic resonators and their application to measurement of parameters. J. Acoust. Soc. Am. 1976, 41: 974-980.

[34] Du X, Chen I. Ferroelectric thin films of bismuth-containing layered perovskites: part II, PbBi2Nb2O9. J. Am. Ceram. Soc. 1998, 81: 3260-3264.

Just Accepted

[35] Newnham RE, Wolfe RW, Dorrian JF. Structural basis of ferroelectricity in the bismuth titanate family. Mater. Res. Bull. 1971, 6: 1029-1039.

[36] Hou Q, Yang B, Ma C, et al. Tailoring structure and piezoelectric properties of CaBi2Nb2O9 ceramics by W6+-doping. Ceram. Int. 2022, 48: 16677-16684.

[37] Wendari TP, Arief S, Mufti N, et al. Structure-property relationships in the lanthanide-substituted PbBi2Nb2O9 Aurivillius phase synthesized by the molten salt method. J. Alloys Compd. 2021, 860: 158440.

[38] Li Z, Yang M, Park JS, et al. Stabilizing perovskite structures by tuning tolerance factor: formation of formamidinium and cesium lead iodide solid-state alloys. Chem. Mater. 2016, 28: 284-292.

[39] Suárez DY, Reaney IM, Lee WE. Relation between tolerance factor and TC in Aurivillius compounds. J. Mater. Res. 2001, 16: 3139-3149.

[40] Rubio-Marcos F, Bañares MA, Romero JJ, et al. Correlation between the piezoelectric properties and the structure of lead-free KNN-modified ceramics, studied by Raman spectroscopy. J. Raman Spectrosc. 2011, 42: 639-643.

[41] Namade L D, Patil A R, Bodake T R, et al. Electroforming−free resistive switching in spray−deposited $SrTiO_3$ thin films with time series analysis for memory devices. Mater. Res. Bull. 2026, 202: 114197.

[42] Morgan D J. Photoelectron spectroscopy of ceria: Reduction, quantification and the myth of the vacancy peak in XPS analysis. Surf. Interface Anal. 2023, 55: 845-850.

[43] Chen N, Wang F, Li X, et al. Improving the piezoelectric properties of CBN-based ceramic by a Ce ion. J. Am. Ceram. Soc. 2022, 105: 6207-6216.

[44] Qin C, Shen Z, Luo W, et al. Microstructure related properties enhancing in Ce-doped CaBi2Nb2O9 high temperature piezoelectric ceramics. Mater. Res. Express 2019, 6: 106308.

[45] Wang M, Zhang Y, Luo X, et al. Enhancement of piezoelectric properties with high Curie temperature in CaBi2Nb2O9 via MnO2 doping. Trans. Nonferrous Met. Soc. China 2025, 35: 552-562.

[46] Jie S, Jiang X, Chen C, et al. Influence of Co/W co-doping on structural and electrical properties of Na0.5Bi2.5Nb2O9 piezoelectric ceramics. Ceram. Int. 2022, 48: 6258-6265.

[47] Raddaoui Z, El Kossi S, Dhahri J, et al. Study of diffuse phase transition and relaxor ferroelectric behavior of Ba0.97Bi0.02Ti0.9Zr0.05Nb0.04O3 ceramic. RSC Adv. 2019, 9: 2412-2425.

Just Accepted

[48] Wang J, Wang S, Li X, et al. High piezoelectricity and low strain hysteresis in PMN-PT-based piezoelectric ceramics. J. Adv. Ceram. 2023, 12: 792-802.
[49] Trigui W, Hlel F. Ferroelectric properties and Raman spectroscopy of the [(C4H9)4N]3Bi2Cl9 compound. RSC Adv. 2019, 9: 24291-24298.
[50] Bishop AR, Bussmann-Holder A, Kamba S, et al. Common characteristics of displacive and relaxor ferroelectrics. Phys. Rev. B 2010, 81: 064106.
[51] Du H, Ma C, Ma W, et al. Microstructure evolution and dielectric properties of Ce-doped SrBi4Ti4O15 ceramics synthesized via glycine-nitrate process. Process. Appl. Ceram. 2018, 12: 303-312.
[52] Zhou Z, Duan X, Chen Y. Synergistically enhancing the electrical resistivity and thermal stability of Bi4Ti3O12 ceramics by multiple-ions doping of Ce/W/Mo. Ceram. Int. 2025, 51: 36388-36400.
[53] Li W, Hao J, Li W, et al. Electrical properties and luminescence properties of 0.96(K0.48Na0.52)(Nb0.95Sb0.05)-0.04Bi0.5(Na0.82K0.18)0.5ZrO3-xSm lead-free ceramics. J. Adv. Ceram. 2020, 9: 72-82.
[54] Wong Y, Hassan J, Hashim M. Dielectric properties, impedance analysis and modulus behavior of CaTiO3 ceramic prepared by solid state reaction. J. Alloys Compd. 2013, 571: 138-144.
[55] Morrison FD, Sinclair DC, West AR. Characterization of lanthanum-doped barium titanate ceramics using impedance spectroscopy. J. Am. Ceram. Soc. 2001, 84: 531-538.
[56] Mahamoud H, Louati B, Hlel F, et al. Impedance and modulus analysis of the (Na0.6Ag0.4)2PbP2O7 compound. J. Alloys Compd. 2011, 509: 6083-6089.
[57] Mohanty V, Cheruku R, Vijayan L, et al. Ce-substituted lithium ferrite: preparation and electrical relaxation studies. J. Mater. Sci. Technol. 2014, 30: 335-341.
[58] Jonscher AK. The "universal" dielectric response. Nature 1977, 267: 673-679.
[59] Elliott SR. Temperature dependence of ac conductivity of chalcogenide glasses. Philos. Mag. B 1978, 37: 553-560.
[60] Mohamed CB, Karoui K, Saidi S, et al. Electrical properties, phase transitions and conduction mechanisms of the [(C2H5)NH3]2CdCl4 compound. Physica B 2014, 451: 87-95.
[61] Chen H, Guo X, Cui Z, et al. Donor and acceptor doping effects on the electrical conductivity of $CaBi_2Nb_2O_9$ ceramics. Phys. Status Solidi A 2013, 210: 1121-1127.
[62] Hooper TE, Roscow JI, Mathieson A, et al. High voltage coefficient piezoelectric materials and their applications. J. Eur. Ceram. Soc. 2021, 41: 6115-6129.
[63] Schultheiß J, Checchia S, Uršič H, et al. Domain wall–grain boundary interactions in polycrystalline $Pb(Zr_{0.7}Ti_{0.3})O_3$ piezoceramics. J Eur Ceram Soc 2020, 40(12): 3965–3973.
[64] Yu C, Miao C, Xie S, et al. Microstructural evolutions, elastic properties and mechanical

Just Accepted

behaviors of W/Cr co-doped $Bi_4Ti_3O_{12}$ ceramics. Mater Des 2016, 90: 628–634.

Just Accepted